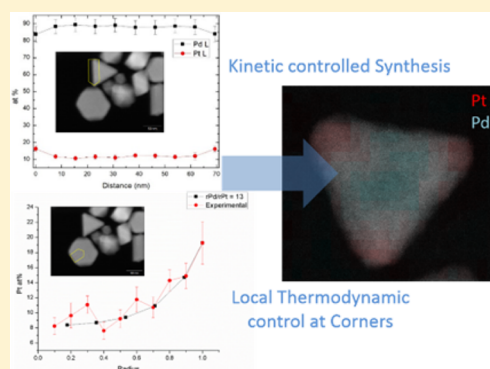


# Compositional Inhomogeneity and Corner Enrichment of Pt in Pt/Pd Bimetallic Nanoparticles

Lingxuan Peng,<sup>†</sup> Richard P. Van Duyne,<sup>‡</sup> and Laurence D. Marks<sup>\*,†</sup><sup>†</sup>Department of Materials Science and Engineering and <sup>‡</sup>Department of Chemistry, Northwestern University, Evanston, Illinois 60208, United States

## Supporting Information

**ABSTRACT:** Experimental results of a smooth composition gradient within Pt/Pd alloy nanoparticles with Pt enrichment at the corners are reported. We find that the Pt concentration gradually increases toward the outermost surface, and it appears different from the thermodynamically most stable configuration. We demonstrate that it is the result of reaction kinetics of both the reduction of precursors and growth of nanoparticles, by a growth model. We then explain that the corner Pt enrichment is a result of local thermodynamic control at the corners. This mixed control of kinetics and thermodynamics in bimetallic nanoparticle synthesis can lead to the formation of particles with a complex concentration profile, which could be interesting when these particles are used in catalytic applications. Our analysis is not simply a qualitative model but rather a relatively rigorous quantitative analysis of the composition as a function of the growth conditions, which can serve as a basis for improved reproducibility of synthesis for applications.



## INTRODUCTION

Metal nanoparticles are of interest due to their unique optical, electrical, and catalytic properties, which are different from their monometallic counterparts, and are widely used in various applications.<sup>1–3</sup> Their unique physical and chemical properties are dependent on their size, structure, and composition.<sup>4–8</sup> Changes in the composition of bimetallic nanoparticles enables tuning of the chemical and physical properties of these particles, for instance, the localized surface plasmon resonance (LSPR).<sup>9,10</sup> Many studies have been focused on their catalytic behaviors. They offer distinct activities and selectivities different and often better than those of their monometallic counterparts.<sup>11–15</sup> It has been shown in the literature that surface segregation (that is, deviation of surface composition from the bulk) affects the chemical properties of the surface and its performance as a catalyst for several reactions.<sup>16–18</sup> There are recent review articles summarizing how segregation has been predicted theoretically and computationally, as well as providing experimental examples.<sup>6,15,19</sup>

Most analytical and computational models give the thermodynamically most stable structure; however, many syntheses are kinetically controlled and correspond to kinetic-Wulff shapes, as recently reviewed in detail.<sup>20</sup> In this paper, we demonstrate a kinetics-driven compositional gradient inside of Pt/Pd bimetallic multiply twinned particles. Pt/Pd bimetallic nanoparticles are of interest owing to their importance in catalysis.<sup>21–23</sup> A gradual increase of Pt within the particle from the center to the outermost surface and an enrichment of Pt at the corners are observed, which is a result of a local thermodynamic control at the corners. We first show via

analytical modeling that the compositional gradient is a result of Pt and Pd having different growth rates. We then show that the corner concentration is related to the weighted mean curvature (wmc, chemical potential) of the corner and indicates that the corner concentration of Pt is a function of Pt and Pd chemical potential in solution. Our analysis is not simply a qualitative model but rather a relatively rigorous quantitative analysis of the composition as a function of the growth conditions, which can serve as a basis for improved reproducibility of synthesis for applications.

## EXPERIMENTAL PROCEDURE

Synthesis of Pt/Pd alloy multiply twinned particles was performed via a method developed by Lim et al.<sup>24</sup> The ratio of Pt and Pd precursors was modified to yield Pt/Pd alloy nanoparticles with different overall concentrations and different degrees of Pt corner enrichment. Poly(vinylpyrrolidone) (PVP, 70 mg, MW  $\approx$  55000) was dissolved in 16 mL of deionized water and was heated to 80 °C in air. Different molar ratios of sodium tetrachloropalladate(II) ( $\text{Na}_2\text{PdCl}_4$ ) and potassium tetrachloroplatinate(II) ( $\text{K}_2\text{PtCl}_4$ ) were dissolved in 6 mL of deionized water at room temperature. For a 1:1 molar ratio solution, 0.032 mmol of  $\text{Na}_2\text{PdCl}_4$  and 0.032 mmol  $\text{K}_2\text{PtCl}_4$  were used. The  $\text{Na}_2\text{PdCl}_4$  and  $\text{K}_2\text{PtCl}_4$  solution was then added

**Special Issue:** Richard P. Van Duyne Festschrift

**Received:** April 8, 2016

**Revised:** July 2, 2016

to the PVP aqueous solution, and the mixture was allowed to react at 80 °C for 18 h.

The Pt/Pd alloy nanoparticles were washed five times and deposited onto ultrathin carbon grids. The morphology of the nanoparticles was characterized using a JEOL 2100F transmission electron microscope (TEM) and high-angle annular dark field (HAADF) imaging in an aberration-corrected JEOL JEM-ARM200F scanning transmission electron microscope (STEM). The 2D projection of the elemental distribution within the particles was characterized via energy-dispersive X-ray spectroscopy (EDX) using both a Hitachi HD2300 and the JEOL JEM-ARM200F STEM. In situ heating experiments were performed using the JEOL 2100F microscope.

We note that the spatial resolution of EDX is dependent on the acceleration voltage and the sample thickness and geometry. In the STEM, the acceleration voltage was 200 kV, which was rather high and would lead to a small interaction volume in thin samples (confirmed by standard Monte Carlo simulations, not shown). The composition quantified from EDX spectra is a 2D projection of the 3D elemental distribution inside of the particles.

## RESULTS

The product includes different multiply twinned particles, such as truncated/untruncated bipyramids, Marks decahedra (Dh), icosahedra (Ic), and hexagonal platelets. The morphologies of the as-synthesized particles are shown in Figure 1.

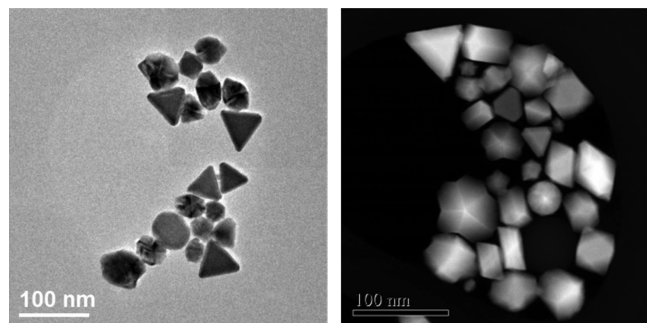


**Figure 1.** TEM and HAADF images of Pt/Pd multiply twinned particles made by a 1:1 molar ratio of Pd and Pt precursors.

The linescans from the corner to the bulk and between two corners indicate Pt enrichment at the surface, especially at the corners. The measured EDX composition profiles of particles synthesized with different precursor ratios as a function of distance from the center to the surface are shown in Figure 2 together with modeling results, which will be discussed later. In all cases they show an increase in the Pt concentration away from the center, not simply surface segregation of Pt. A related result is shown in Figure 3, a two-dimensional EDX map of a nanoparticle synthesized using a 1:1 molar ratio of Pt and Pd precursors. In addition to the radial composition shown in Figure 2, there is an additional increase in the Pt concentration at corners. This was reproducible and observed for more than 50 different nanoparticles for this composition of the precursors and other.

**Model for Radial Concentration Change.** As reviewed recently,<sup>20</sup> the shape of nanoparticles with flat facets can be described in terms of either thermodynamic or kinetic Wulff constructions. We now seek to establish a model based on these established methods that will account for the concentration

profiles. As shown in Figures 2 and 3, the Pt concentration increased toward the surface, and there are three possible explanations for this. The simplest possibility is that the nanoparticles were in their thermodynamic stable configurations and the element with lower surface energy segregated to the surface. It is well-established that surface energy can play an important role in determining the surface composition in alloy systems.<sup>15,19,25,26</sup> For instance, Williams and Nason developed a thermodynamic model predicting surface segregation based on minimizing the surface energy by allowing atoms to exchange between surface layers and the bulk. They suggested that within four atomic layers, the composition becomes constant.<sup>25</sup> In the same model, they analyzed the effect of chemisorption and size and compared the model with experimental results.<sup>27–29</sup> The same method has been used for predicting the surface segregation in Au/Ag bimetallic nanoparticles.<sup>30</sup> More recent works have shown that in nanoparticle systems, the surface composition can be altered by chemisorption.<sup>17,31–33</sup> For the specific case of Pd/Pt, there are experimental and computational results showing that Pd tends to segregate to the surface.<sup>32,34,35</sup> According to a recent thermodynamic model,<sup>26</sup> there is a balance between the decrease in surface energy and increase in bulk free energy, which prevents full surface segregation of species to the surface. In such a case, we expect that there would be just surface segregation on an otherwise homogeneous bulk alloy nanoparticle. This is not consistent with the present experimental results.

A second possibility is that the concentration gradients are a consequence of interdiffusion within the nanoparticles. One indicator of this would be Kirkendall voids;<sup>36–38</sup> none were observed. A more definitive test was an in situ heating of the sample within an electron microscope to a temperature of approximately 700 °C for 90 min. There was no evidence of any additional surface segregation or change in the composition, indicating that interdiffusion is not dominant even at such high temperatures. Since the synthesis is conducted at a much lower temperature (80 °C), it is unlikely that these concentration gradients are a result of interdiffusion during synthesis.

The third possibility is that the compositional gradient was not from segregation within the particle but from the growth kinetics. That growth kinetics can be critical has been known since the early work of Berg,<sup>39</sup> as we have discussed in a recent review.<sup>20</sup> Because the concentrations of both the Pt and Pd in solution are finite, this will lead to a gradual change in the composition, which is consistent with the experimental data. This type of model has been proposed in the existing literature; for instance, Ahrenstorf et al. studied the mechanism of formation of Ni/Pt bimetallic nanoparticles and demonstrated that Pt and Ni precursors had different consumption rates,<sup>40</sup> while Choi et al. studied the formation mechanism of Pt/Ni octahedra and demonstrated control of the composition by varying the amount of solvent, precursors, and surfactant added,<sup>41</sup> and they observed the concentration of Pt being richer at the edges and vertices than that at the center and suggested that the amine group in oleylamine could coordinate with Pt(acac)<sub>2</sub> in the initial stage of the synthesis.<sup>42</sup> However, quantitative comparisons are currently lacking to substantiate this model.

To develop a model, we first define what is taking place. The PVP is used as the reducing agent. As PdCl<sub>4</sub><sup>2-</sup> and PtCl<sub>4</sub><sup>2-</sup> are reduced to Pd and Pt monomers, and the nucleation stage begins and is followed by growth after the nuclei have reached a

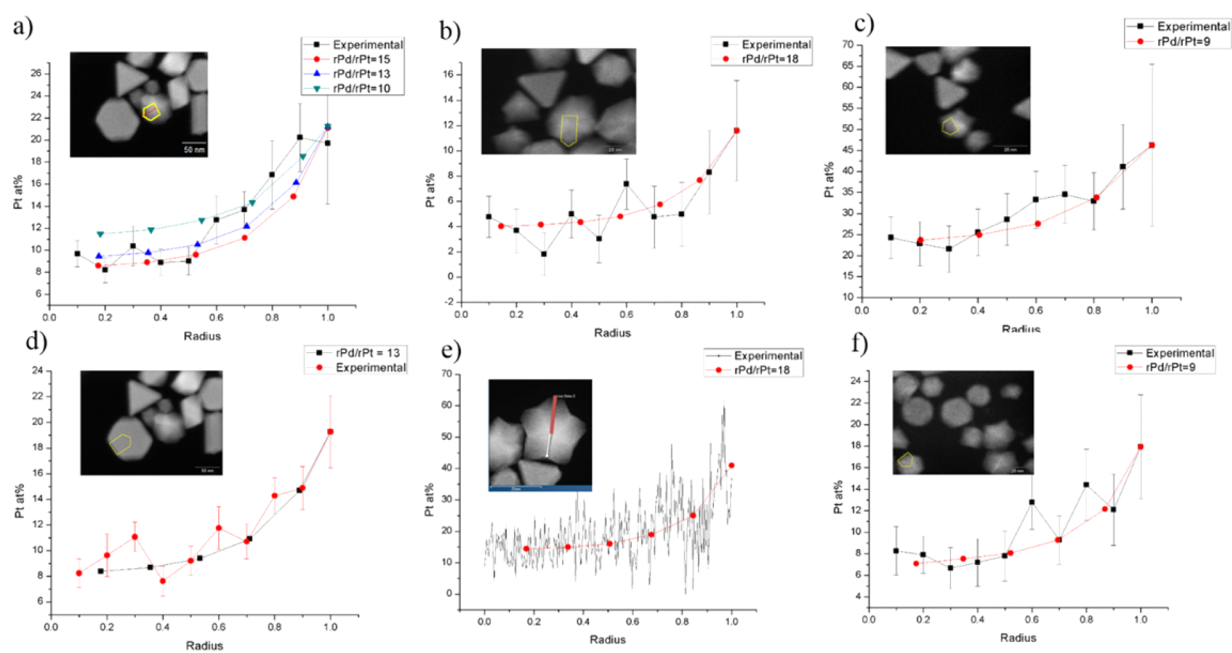


**Figure 2.** Measured composition profile and calculated 2D projection as a function of distance from the center to the surface. (a) The composition profile of a decahedron fitted with a different  $r_{Pd}(T)/r_{Pt}(T)$  ratio; (a) and (d) are composition profiles of a particle synthesized with a 1:1 molar ratio of Pd and Pt precursors. (b) Composition profile of a particle synthesized with a double amount of Pd. (e) Composition profile of a particle synthesized with a double amount of Pt (highlighted in red in the HAADF image). The composition profiles of the particles in (b) and (e) have the same  $r_{Pd}(T)/r_{Pt}(T)$  ratio. (c) Composition profile of a particle synthesized with half of the amount of Pd. (f) Composition profile of a particle synthesized with half of the amount of Pt. The composition profiles of the particle in (c) and (f) have the same  $r_{Pd}(T)/r_{Pt}(T)$  ratio.

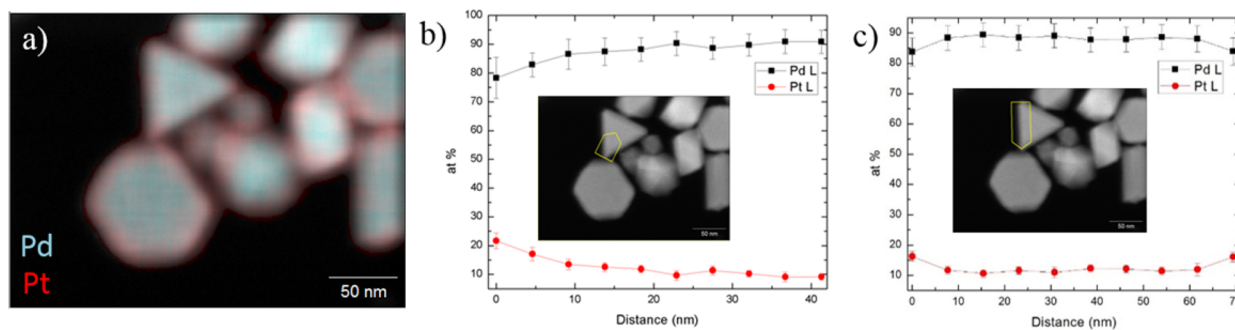


**Figure 3.** EDX measurements showing the surface and corner enhancement of Pt in Pt/Pd bimetallic nanoparticles. (a) The EDX elemental maps of the Pd/Pt multiply twinned particles. (b) The EDX linescan from the corner to the center of a particle. (c) The EDX linescan between two corners of the same particle.

critical size. The final products had well-defined facets, suggesting that the growth was interface-controlled, that is, was a kinetic-Wulff mode.<sup>20,43,44</sup> The schematics of the formation of these particles is shown in Figure 4. For interface-controlled growth, the rate of growth is limited by the rate of atoms moving from region II to region III in Figure 4a.<sup>20</sup> There are monatomic terraces nucleated on an existing flat surface, followed by the growth of this terrace across the facet. According to classical nucleation theory, after the nucleation of the monatomic terrace, the contribution of the bulk free energy will dominate, and the growth of this terrace will be spontaneous and fast as the free energy of the terrace formation will be negative.

The nanoparticle formation was separated into two steps, reduction of precursors and growth of nanoparticles, because the reduction and growth were on two different time scales. The core of the synthesized nanoparticles had higher Pd concentration, and it gradually decreased toward the surface. It

indicated that the deposition rate of Pd was higher than that of Pt. The deposition rate had contributions from both reduction of precursors and deposition of reduced monomers.

As the particle grew beyond the critical nucleation size, it was relatively stable and started to grow. The growth was from the flux of the Pt and Pd atoms in the supersaturated solution depositing onto the nanoparticle surface.

The reduction rates are written as

$$r(\text{Pd}) = k_{Pd}(T)[\text{PdCl}_4^{2-}][\text{PVP}]^2 \quad (1)$$

$$r(\text{Pt}) = k_{Pt}(T)[\text{PtCl}_4^{2-}][\text{PVP}]^2 \quad (2)$$

where  $r(\text{Pd})$  and  $r(\text{Pt})$  are the reaction rate of the reduction of Pd and Pt precursors;  $k_{Pd}(T)$  and  $k_{Pt}(T)$  are the reaction rate constants that are dependent upon temperature but independent of reactant concentrations;  $[\text{PdCl}_4^{2-}]$  and  $[\text{PtCl}_4^{2-}]$  are the concentrations of Pd and Pt precursors. The reaction temperature was held constant during the reaction; therefore,

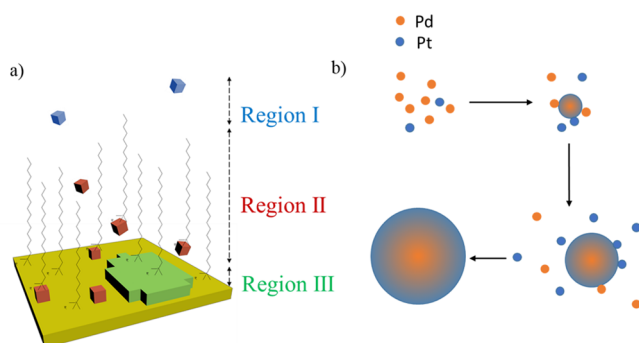


**Figure 4.** Schematics of nanoparticle formation. (a) The regions for kinetic growth. Region I contains external Pt and Pd atoms that are reduced by PVP, region II Pt and Pd atoms that diffuse to the terrace, and region III a nucleating terrace. (b) Schematic explaining the origin of the concentration gradient. The Pd atoms attach to the surface faster than Pt atoms, and as growth proceeds, Pd atoms are consumed faster than Pt atoms and more Pt is deposited near the surface of the particles.

we will assume that  $k_{\text{Pd}}(T)$  and  $k_{\text{Pt}}(T)$  are constant for this particular synthesis and will be written as  $k_{\text{Pd}}$  and  $k_{\text{Pt}}$  later on.

The Arrhenius equation gives a quantitative definition of the reaction rate constant. Simplifying that the nanoparticles have spherical shapes (which we will return to later), we used a simple collision model, and the ratio between  $k_{\text{Pd}}$  and  $k_{\text{Pt}}$  was determined to be 1.035; the details are included in the [Supporting Information](#).

The deposition rates  $R_{\text{Pt}}(T)$  and  $R_{\text{Pd}}(T)$  are proportional to the product of deposition rate constants,  $r_{\text{Pt}}(T)$  and  $r_{\text{Pd}}(T)$  and the concentration of reduced Pt and Pd monomers. Our observation indicated that Pd had a higher deposition rate and Pd atoms attached to the surface faster than Pt, resulting in a Pd-rich core. As growth proceeded, Pd atoms were consumed faster than Pt, and more Pt was deposited near the surface of the nanoparticles and left a concentration gradient inside of the particles.

The concentration profiles were dependent upon the reduction and deposition rates of Pd and Pt and the incubation time (the nucleation period). The incubation period and ratio between the reduction and deposition rates were determined to have minimal effects on the concentration profile, and the detailed comparisons can be found in the [Supporting Information](#). An approximation was used here that the bigger particles grew at an earlier time than the smaller ones, and all of the particles in the solution stopped growing at the same time (18 h).

To compare with the experimental results ([Figure 2](#)), we first calculated the three-dimensional concentration profile assuming spherical particles and the reaction kinetics outlined above and then numerically integrated the composition of Pt as a function of distance along the beam direction (to match the projected EDX results). We then adjusted the  $r_{\text{Pd}}(T)/r_{\text{Pt}}(T)$  ratio to obtain reasonable fits to the experimental data using 12 different measurements. We found that the ratio obtained from the best fits varies with the total amount of precursor molecules added during synthesis. The  $r_{\text{Pd}}(T)/r_{\text{Pt}}(T)$  ratio as a function of the sum of Pt and Pd precursor concentrations is plotted in [Figure 5](#). The syntheses had the same  $r_{\text{Pd}}(T)/r_{\text{Pt}}(T)$  ratio by adding half of the Pd precursors (Pd/Pt precursor = 1:2) and half of the Pt precursor (Pd/Pt precursor = 2:1), and doubling the amount of Pd precursor and Pt precursor resulted in the

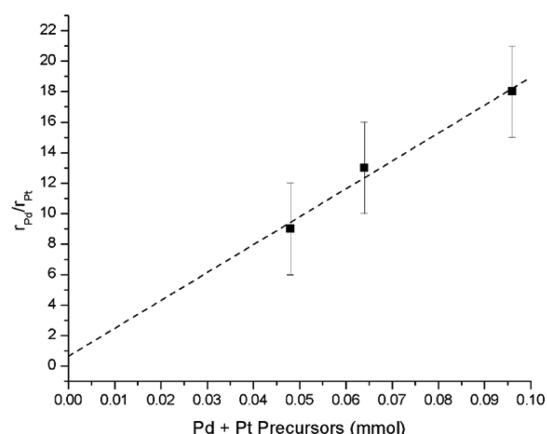


**Figure 5.**  $r_{\text{Pd}}(T)/r_{\text{Pt}}(T)$  as a function of the total amount of Pd and Pt precursor concentration.

same  $r_{\text{Pd}}(T)/r_{\text{Pt}}(T)$  value. The deposition rate constant was independent of the concentration of each precursor but dependent upon the total precursor concentration. As the total precursor concentration increases, the  $r_{\text{Pd}}(T)/r_{\text{Pt}}(T)$  ratio will increase.

As we mentioned above, the shapes of the nanoparticles are not spheres; therefore, we compared the  $r_{\text{Pd}}(T)/r_{\text{Pt}}(T)$  ratio between truncated bipyramids and Marks decahedra synthesized under the same conditions, and they appear to be similar. The results that we obtained from fitting the data with a spherical model might differ from the real  $r_{\text{Pd}}(T)/r_{\text{Pt}}(T)$  ratio, but it is consistent between two dominant shapes in the synthesis.

**Model for Pt Enhancement at the Corners.** Another important observation was that the Pt concentration was higher at the corners than that on the surface. To explain this phenomenon, a concept of weighted mean curvature (wmc) should be introduced.<sup>44</sup> The wmc is the ratio of the change in surface energy and the change in volume. For a simple corner, the chemical potential at an apex can be written as the ratio between the weighted mean surface energy and the truncation along the plane normal. Therefore, the chemical potential goes toward infinity for sharp corners and it is not an artifact of a continuum model as it was verified by density functional calculations. A Lyapunov stable solution will be reached when the external chemical potential equals the chemical potential at the truncated corner.

This Lyapunov stable solution can be extended to the alloy case. This is also analogous to the Stefan problem. At the corner, the differential equation as a function of chemical potentials will be

$$\frac{ds}{dt} = -a(\mu(x_{\text{Pt}}) - x_{\text{Pt}}\mu^{\text{ext}}(\text{Pt}) - (1 - x_{\text{Pt}})\mu^{\text{ext}}(\text{Pd})) \quad (3)$$

where  $s$  is the boundary of the corner,  $a$  is a constant,  $\mu^{\text{ext}}$  is the external chemical potential, and  $\mu(x_{\text{Pt}})$  is the chemical potential of the corner as a function of the concentration of Pt at the corner, which can be written as<sup>44</sup>

$$\mu(x_{\text{Pt}}) = \frac{\Omega_0(x_{\text{Pt}}\bar{\gamma}_{\text{Pt}} + (1 - x_{\text{Pt}})\bar{\gamma}_{\text{Pd}})}{L - h} \quad (4)$$

where  $L$  is the distance from the Wulff center to the apex of a corner and  $h$  is the distance from the Wulff center to the truncated surface at a corner;  $\Omega_0$  is the atomic volume, and  $\bar{\gamma}_{\text{Pt}}$

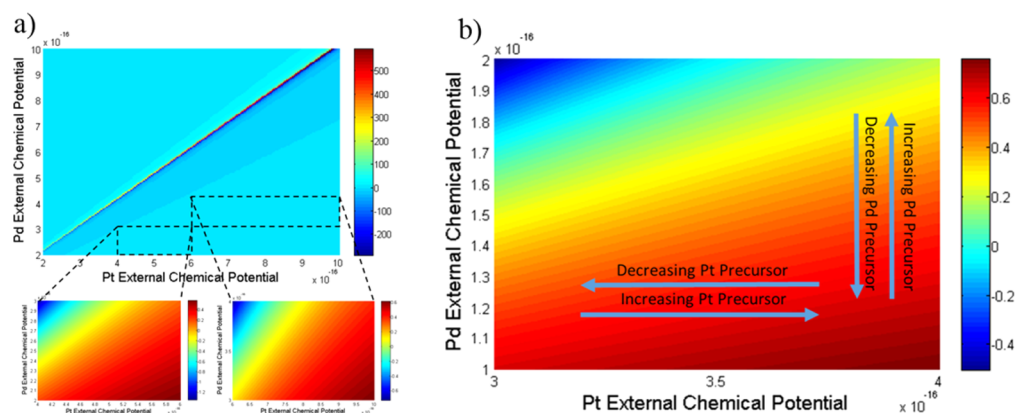


**Figure 6.** (a) Corner concentration of Pt as a functions of the Pd and Pt external chemical potential. (b) Zoomed-in Pt corner concentration map showing how the Pt corner concentration changes with Pt and Pd precursor concentrations.

and  $\bar{\gamma}_{\text{Pd}}$  are the weighted mean surface energies of Pt and Pd, assuming that the surface energy of the Pt/Pd alloy varies linearly between Pt and Pd. The Lyapunov solution is then

$$x_{\text{Pt}} = 1 - \frac{C\mu^{\text{ext}}(\text{Pd}) - \bar{\gamma}_{\text{Pt}}}{C[\mu^{\text{ext}}(\text{Pt}) - \mu^{\text{ext}}(\text{Pd})] + \bar{\gamma}_{\text{Pd}}} \quad (5)$$

where

$$C = \frac{L - h}{\Omega_0} \quad (6)$$

The Pt concentration at the corner is plotted as functions of external chemical potentials of Pd and Pt in Figure 6.

The external chemical potential is a function of the Pt and Pd monomer concentrations, and it can be written as

$$\mu_i = \mu_0 + RT \ln a_i = \mu_0 + RT \ln \gamma \frac{b_i}{b_0} \quad (7)$$

where  $\mu_0$  is the standard chemical potential of a species,  $a_i$  the activity of the species,  $\gamma$  the activity coefficient,  $b_i$  the molality, and  $b_0$  the standard molality.

Figure 6b shows that with increasing Pd precursor and decreasing Pt precursor concentrations in solution, the concentration of Pt at the corners decreases. In contrast, as the Pd precursor concentration decreases or as the Pt precursor concentration increases in solution, the Pt corner concentration increases. This is consistent with the observed corner Pt concentrations with different amount of precursors added.

## DISCUSSION

The evidence indicates that for the synthetic conditions herein we have a mixture of control via the reaction kinetics that form the two different monomers and the reaction kinetics of growth with local thermodynamic control at the corners. This is a natural extension of existing models that are well-established in the literature.<sup>20,44</sup> Such a combination may be of general relevance in many other cases of alloy nanoparticle solution growth; we leave this hypothesis to further work.

From our analysis, the deposition rate constant  $r_{\text{Pd}}(T)/r_{\text{Pt}}(T)$  ratio ranges from 9 to 18 at different synthesis conditions, and the reduction rate constant ratio  $k_{\text{Pd}}/k_{\text{Pt}}$  is around 1. This implies that the presence of PVP slows down the Pt deposition rate. This is consistent with spectroscopic data where there is a larger peak shift of C=O in FTIR spectra for PVP–Pt compared to PVP–Pd.<sup>45</sup> The stronger interaction between Pt

and PVP slows down the deposition of Pt, and thus, Pd is preferentially deposited onto the surface of the nanoparticles. The concentration of capped PVP at the corners is lower than that at the surface, which results in higher Pt concentration at the corners.

It worth mentioning that the degree of corner enrichment also depends on the amount of PVP used during synthesis. We can define the degree of corner enrichment as (corner concentration – central bulk concentration)/central bulk concentration. By changing the amount of PVP from the amount reported in the [Experimental Procedure](#) section, the degrees of corner enrichment for 50, 100, and 200% PVP are 35, 100, and 150%, respectively. The corner concentrations (8, 18, and 50% of Pt) represents the external chemical potential; however, the kinetics still controls the elemental distribution elsewhere. Changing the amount of PVP in this particular reaction can also yield higher corner concentration of Pt. However, the surface appears to be rougher with increasing PVP concentration, which indicates that more  $\text{Cl}^-$  ions are produced in solution during reduction and thus the etching from  $\text{Cl}^-$  is more severe for the particles synthesized with a larger amount of PVP added.

There are a lot of mechanistic studies on bimetallic nanoparticle formation of different systems present in the literature. Ahrenstorf et al. studied the mechanism of formation of Ni/Pt bimetallic nanoparticles and demonstrated that Pt and Ni precursors had different consumption rates.<sup>40</sup> Choi et al. systematically studied the formation mechanism of Pt/Ni octahedra and demonstrated the controlling of the size and composition by varying the amount of solvent, precursors, and surfactant added.<sup>41</sup> Pt/Ru alloy particle formation was also claimed as a result of interdiffusion between a core–shell-like structure, which was formed from two-step nucleation.<sup>46</sup> Interdiffusion was discussed as a possibility and was found not to be the case in our system by postannealing. Yin et al. had seen Pd/Ag nanoparticles with highly twinned structures formed by coalescence and agglomeration.<sup>47</sup> In our model, we analyzed the compositional profile in detail and proposed a new model showing the coexist of kinetic and thermodynamic controls, and it helps understand the inhomogeneous elemental distribution in bimetallic nanoparticles and would be beneficial for rational design of novel catalysts.

## CONCLUSION

We demonstrated that the smooth composition gradient within the particle is the result of reaction kinetics of monomer formation and growth of particles. The deposition rate constant ratio  $r_{\text{Pd}}(T)/r_{\text{Pt}}(T)$  is a function of the total amount of precursors and is independent of the ratio between Pt and Pd precursors added. The corner Pt enrichment is a result of local thermodynamic control at the corners. The mixed control of kinetics and thermodynamics in bimetallic nanoparticle synthesis can provide particles with complex composition distribution within the particles. More generally, there are opportunities to design novel bimetallic catalysts utilizing local elemental enrichments at the corners, where there are more active sites for a variety of catalytic reactions.

## ASSOCIATED CONTENT

### Supporting Information

The Supporting Information is available free of charge on the ACS Publications website at DOI: 10.1021/acs.jpcc.6b03609.

Calculation of  $k_{\text{Pt}}(T)/k_{\text{Pd}}(T)$  and effect of the incubation period and ratio between the deposition rates on the Pt concentration profile (PDF)

## AUTHOR INFORMATION

### Corresponding Author

\*E-mail: l-marks@northwestern.edu. Phone: 847-491-3996.

### Notes

The authors declare no competing financial interest.

## ACKNOWLEDGMENTS

This work was supported by the Materials Research Center (MRSEC) at Northwestern University, on the grant DMR-1121262. The MRSEC is funded by the National Science Foundation.

## REFERENCES

- (1) Henry, A.-I.; Bingham, J. M.; Ringe, E.; Marks, L. D.; Schatz, G. C.; Van Duyne, R. P. Correlated Structure and Optical Property Studies of Plasmonic Nanoparticles. *J. Phys. Chem. C* **2011**, *115*, 9291–9305.
- (2) Talapin, D. V.; Lee, J.-S.; Kovalenko, M. V.; Shevchenko, E. V. Prospects of Colloidal Nanocrystals for Electronic and Optoelectronic Applications. *Chem. Rev.* **2010**, *110*, 389–458.
- (3) Burda, C.; Chen, X.; Narayanan, R.; El-Sayed, M. A. Chemistry and Properties of Nanocrystals of Different Shapes. *Chem. Rev.* **2005**, *105*, 1025–1102.
- (4) Ringe, E.; Langille, M. R.; Sohn, K.; Zhang, J.; Huang, J.; Mirkin, C. A.; Van Duyne, R. P.; Marks, L. D. Plasmon Length: A Universal Parameter to Describe Size Effects in Gold Nanoparticles. *J. Phys. Chem. Lett.* **2012**, *3*, 1479–1483.
- (5) Hua, Y.; Chandra, K.; Dam, D. H. M.; Wiederrecht, G. P.; Odum, T. W. Shape-Dependent Nonlinear Optical Properties of Anisotropic Gold Nanoparticles. *J. Phys. Chem. Lett.* **2015**, *6*, 4904–4908.
- (6) Ferrando, R.; Jellinek, J.; Johnston, R. L. Nanoalloys: From Theory to Applications of Alloy Clusters and Nanoparticles. *Chem. Rev.* **2008**, *108*, 845–910.
- (7) Guisbiers, G.; Abudukelimu, G.; Hourlier, D. Size-Dependent Catalytic and Melting Properties of Platinum-Palladium Nanoparticles. *Nanoscale Res. Lett.* **2011**, *6*, 396.
- (8) Narayanan, R.; El-Sayed, M. A. Shape-Dependent Catalytic Activity of Platinum Nanoparticles in Colloidal Solution. *Nano Lett.* **2004**, *4*, 1343–1348.
- (9) Motl, N. E.; Ewusi-Annan, E.; Sines, I. T.; Jensen, L.; Schaak, R. E. Au–Cu Alloy Nanoparticles with Tunable Compositions and

Plasmonic Properties: Experimental Determination of Composition and Correlation with Theory. *J. Phys. Chem. C* **2010**, *114*, 19263–19269.

(10) Wilcoxon, J. Optical Absorption Properties of Dispersed Gold and Silver Alloy Nanoparticles. *J. Phys. Chem. B* **2009**, *113*, 2647–2656.

(11) Sankar, M.; Dimitratos, N.; Miedzkiak, P. J.; Wells, P. P.; Kiely, C. J.; Hutchings, G. J. Designing Bimetallic Catalysts for a Green and Sustainable Future. *Chem. Soc. Rev.* **2012**, *41*, 8099–8139.

(12) Bracey, C. L.; Ellis, P. R.; Hutchings, G. J. Application of Copper-Gold Alloys in Catalysis: Current Status and Future Perspectives. *Chem. Soc. Rev.* **2009**, *38*, 2231–2243.

(13) Scheidt, W. R. Trends in Metalloporphyrin Stereochemistry. *Acc. Chem. Res.* **1977**, *10*, 339–345.

(14) Singh, A. K.; Xu, Q. Synergistic Catalysis Over Bimetallic Alloy Nanoparticles. *ChemCatChem* **2013**, *5*, 652–676.

(15) Liao, H.; Fisher, A.; Xu, Z. J. Surface Segregation in Bimetallic Nanoparticles: A Critical Issue in Electrocatalyst Engineering. *Small* **2015**, *11*, 3221–3246.

(16) Stamenkovic, V. R.; Mun, B. S.; Mayrhofer, K. J. J.; Ross, P. N.; Markovic, N. M. Effect of Surface Composition on Electronic Structure, Stability, and Electrocatalytic Properties of Pt-Transition Metal Alloys: Pt-Skin Versus Pt-Skeleton Surfaces. *J. Am. Chem. Soc.* **2006**, *128*, 8813–8819.

(17) Suntivich, J.; Xu, Z.; Carlton, C. E.; Kim, J.; Han, B.; Lee, S. W.; Bonnet, N.; Marzari, N.; Allard, L. F.; Gasteiger, H. A.; et al. Surface Composition Tuning of Au–Pt Bimetallic Nanoparticles for Enhanced Carbon Monoxide and Methanol Electro-Oxidation. *J. Am. Chem. Soc.* **2013**, *135*, 7985–7991.

(18) Tan, L.; Wu, X.; Chen, D.; Liu, H.; Meng, X.; Tang, F. Confining Alloy or Core-Shell Au-Pd Bimetallic Nanocrystals in Silica Nanorattles for Enhanced Catalytic Performance. *J. Mater. Chem. A* **2013**, *1*, 10382–10388.

(19) Peng, L.; Ringe, E.; Van Duyne, R. P.; Marks, L. D. Segregation in Bimetallic Nanoparticles. *Phys. Chem. Chem. Phys.* **2015**, *17*, 27940–27951.

(20) Marks, L.; Peng, L. Nanoparticle Shape, Thermodynamics and Kinetics. *J. Phys.: Condens. Matter* **2016**, *28*, 053001.

(21) Rousset, J. L.; Stievano, L.; Cadete Santos Aires, F. J.; Geantet, C.; Renouprez, A. J.; Pellarin, M. Hydrogenation of Tetralin in the Presence of Sulfur Over  $\Gamma$ - $\text{Al}_2\text{O}_3$ -Supported Pt, Pd, and Pd–Pt Model Catalysts. *J. Catal.* **2001**, *202*, 163–168.

(22) Renouprez, A.; Rousset, J. L.; Cadrot, A. M.; Soldo, Y.; Stievano, L. Structure and Catalytic Activity of Palladium–Platinum Aggregates Obtained by Laser Vaporisation of Bulk Alloys. *J. Alloys Compd.* **2001**, *328*, 50–56.

(23) Fujikawa, T.; Idei, K.; Ebihara, T.; Mizuguchi, H.; Usui, K. Aromatic Hydrogenation of Distillates over  $\text{SiO}_2$ - $\text{Al}_2\text{O}_3$ -Supported Noble Metal Catalysts. *Appl. Catal., A* **2000**, *192*, 253–261.

(24) Lim, B.; Wang, J.; Camargo, P. H. C.; Cobley, C. M.; Kim, M. J.; Xia, Y. Twin-Induced Growth of Palladium–Platinum Alloy Nanocrystals. *Angew. Chem., Int. Ed.* **2009**, *48*, 6304–6308.

(25) Williams, F. L.; Nason, D. Binary Alloy Surface Compositions from Bulk Alloy Thermodynamic Data. *Surf. Sci.* **1974**, *45*, 377–408.

(26) Ringe, E.; Van Duyne, R. P.; Marks, L. D. Wulff Construction for Alloy Nanoparticles. *Nano Lett.* **2011**, *11*, 3399–3403.

(27) Quinto, D. T.; Sundaram, V. S.; Robertson, W. D. Auger Spectra of Copper-Nickel Alloys. *Surf. Sci.* **1971**, *28*, 504–516.

(28) Tarnag, M. L.; Wehner, G. K. Alloy Sputtering Studies with in situ Auger Electron Spectroscopy. *J. Appl. Phys.* **1971**, *42*, 2449–2452.

(29) Anderson, J. H.; Conn, P. J.; Brandenberger, S. G. Hydrogen Chemisorption and Surface Composition of Silica-Supported Platinum-Copper Alloys. *J. Catal.* **1970**, *16*, 326–331.

(30) Guisbiers, G.; Mendoza-Cruz, R.; Bazán-Díaz, L.; Velázquez-Salazar, J. J.; Mendoza-Perez, R.; Robledo-Torres, J. A.; Rodríguez-Lopez, J.-L.; Montejano-Carrizales, J. M.; Whetten, R. L.; José-Yacamán, M. Electrum, the Gold–Silver Alloy, from the Bulk Scale to the Nanoscale: Synthesis, Properties, and Segregation Rules. *ACS Nano* **2016**, *10*, 188–198.

- (31) Tao, F.; Grass, M. E.; Zhang, Y.; Butcher, D. R.; Renzas, J. R.; Liu, Z.; Chung, J. Y.; Mun, B. S.; Salmeron, M.; Somorjai, G. A. Reaction-Driven Restructuring of Rh-Pd and Pt-Pd Core-Shell Nanoparticles. *Science* **2008**, *322*, 932–934.
- (32) van den Oetelaar, L. C. A.; Nooij, O. W.; Oerlemans, S.; Denier van der Gon, A. W.; Brongersma, H. H.; Lefferts, L.; Roosenbrand, A. G.; van Veen, J. A. R. Surface Segregation in Supported Pd–Pt Nanoclusters and Alloys. *J. Phys. Chem. B* **1998**, *102*, 3445–3455.
- (33) Li, T.; Bagot, P. A. J.; Marquis, E. A.; Edman Tsang, S. C.; Smith, G. D. W. Atomic Engineering of Platinum Alloy Surfaces. *Ultramicroscopy* **2013**, *132*, 205–211.
- (34) Lloyd, L. D.; Johnston, R. L.; Salhi, S.; Wilson, N. T. Theoretical Investigation of Isomer Stability in Platinum-Palladium Nanoalloy Clusters. *J. Mater. Chem.* **2004**, *14*, 1691–1704.
- (35) Duan, Z.; Wang, G. Monte Carlo Simulation of Surface Segregation Phenomena in Extended and Nanoparticle Surfaces of Pt–Pd Alloys. *J. Phys.: Condens. Matter* **2011**, *23*, 475301.
- (36) Fan, H. J.; Gösele, U.; Zacharias, M. Formation of Nanotubes and Hollow Nanoparticles Based on Kirkendall and Diffusion Processes: A Review. *Small* **2007**, *3*, 1660–1671.
- (37) Lewis, E. A.; Slater, T. J. A.; Prestat, E.; Macedo, A.; O'Brien, P.; Camargo, P. H. C.; Haigh, S. J. Real-Time Imaging and Elemental Mapping of AgAu Nanoparticle Transformations. *Nanoscale* **2014**, *6*, 13598–13605.
- (38) Crosby, L.; Enterkin, J.; Rabuffetti, F.; Poeppelemer, K.; Marks, L. Wulff Shape of Strontium Titanate Nanocuboids. *Surf. Sci.* **2015**, *632*, L22–L25.
- (39) Berg, W. F. Crystal Growth from Solutions. *Proc. R. Soc. London, Ser. A* **1938**, *164*, 79–95.
- (40) Ahrenstorf, K.; Heller, H.; Kornowski, A.; Broekaert, J. A. C.; Weller, H. Nucleation and Growth Mechanism of Ni<sub>x</sub>Pt<sub>1-x</sub> Nanoparticles. *Adv. Funct. Mater.* **2008**, *18*, 3850–3856.
- (41) Choi, S. I.; Xie, S.; Shao, M.; Lu, N.; Guerrero, S.; Odell, J. H.; Park, J.; Wang, J.; Kim, M. J.; Xia, Y. Controlling the Size and Composition of Nanosized Pt–Ni Octahedra to Optimize Their Catalytic Activities toward the Oxygen Reduction Reaction. *ChemSusChem* **2014**, *7*, 1476–1483.
- (42) Choi, S.-I.; Xie, S.; Shao, M.; Odell, J. H.; Lu, N.; Peng, H.-C.; Protsailo, L.; Guerrero, S.; Park, J.; Xia, X.; et al. Synthesis and Characterization of 9 nm Pt–Ni Octahedra with a Record High Activity of 3.3 a/Mgpt for the Oxygen Reduction Reaction. *Nano Lett.* **2013**, *13*, 3420–3425.
- (43) Ringe, E.; Van Duyne, R. P.; Marks, L. D. Kinetic and Thermodynamic Modified Wulff Constructions for Twinned Nanoparticles. *J. Phys. Chem. C* **2013**, *117*, 15859–15870.
- (44) Alpay, D.; Peng, L.; Marks, L. D. Are Nanoparticle Corners Round? *J. Phys. Chem. C* **2015**, *119*, 21018–21023.
- (45) Tu, W.-x.; Zuo, X.-b.; Liu, H.-f. Study on the Interaction Between Polyvinylpyrrolidone and Platinum Metals During the Formation of the Colloidal Metal Nanoparticles. *Chin. J. Polym. Sci.* **2008**, *26*, 23–29.
- (46) Mi, J.-L.; Norby, P.; Bremholm, M.; Becker, J.; Iversen, B. B. The Formation Mechanism of Bimetallic PtRu Alloy Nanoparticles in Solvothermal Synthesis. *Nanoscale* **2015**, *7*, 16170–16174.
- (47) Yin, Z.; Zhang, Y.; Chen, K.; Li, J.; Li, W.; Tang, P.; Zhao, H.; Zhu, Q.; Bao, X.; Ma, D. Monodispersed Bimetallic PdAg Nanoparticles with Twinned Structures: Formation and Enhancement for the Methanol Oxidation. *Sci. Rep.* **2014**, *4*, 4288.